nature communications

Article

https://doi.org/10.1038/s41467-025-66511-3

Robust biodegradable synapse with sub-biological energy and extended memory for intelligent reflexive system

Received: 23 June 2025

Accepted: 6 November 2025

Yoojin Chang[1,2], Sangyun Na[1,2], Yun Goo Ro[1,2], Cheolhong Park[1], Seokhee Jung[1], Yong-Jin Park[1], Min Sub Kwak[1], Jeeyoon Kim[1], Hyeji Oh[1], Jaejun Kim[1] & Hyunhyub Ko[1] ✉

Biodegradable artificial synapses hold great promise for sustainable neuromorphic electronics, yet combining long-term memory, ultralow energy consumption, and mechanical robustness remains challenging. Here, we report a fully biodegradable multilayer artificial synapse (M-AS) composed of crosslinked chitosan–guar gum (CS–GG) ion-active layers (IALs) and a cellulose acetate (CA) ion-binding layer (IBL). This trilayer architecture enhances ion trapping via ion-dipole coupling (IDC) at the IAL–IBL interface, while hydrogen-bonded crosslinking within the CS–GG matrix enhances mechanical and environmental stability. Sodium chloride, embedded in the IALs, serves as a mobile ionic species analogous to biological neurotransmitters, enabling low-voltage ion migration. Upon electrical stimulation, ion migration and dipole alignment induce IDC, leading to partial ion retention and cascade-like postsynaptic current responses that support memory formation. The M-AS supports key synaptic functionalities—including paired-pulse facilitation, short-term and long-term plasticity, multilevel memory encoding, and bidirectional modulation—under sub-millivolt operation. It achieves the longest long-term memory time (5944 s) reported among biodegradable artificial synapses and an energy consumption (0.85 fJ/event) lower than that of biological synapses. Integration with a thermistor and robotic actuator enables a bioinspired reflexive system capable of adaptive, stimulus-dependent learning and reflex-like behaviors. These results demonstrate the potential of M-AS for low-power, intelligent human–machine interfaces.

The human nervous system processes external stimuli through interconnected neurons and synapses, where neurotransmitters are released from presynaptic terminals and bind to receptors on postsynaptic membranes, generating postsynaptic current (PSCs) with remarkably low energy consumption (1–10 fJ per synaptic event)[1–3]. Synaptic plasticity, manifested as short-term plasticity (STP) and long-term plasticity (LTP), enables learning and memory by dynamically modulating PSCs in response to repeated or sustained stimulation[4]. Additional features such as paired-pulse facilitation (PPF) and paired-pulse depression (PPD) serve as quantitative indicators of adaptive signal processing. Inspired by these energy-efficient and adaptive functions, artificial synapses have emerged as key components in neuromorphic electronics. In particular, biopolymer-based artificial synapses are gaining attention due to their mechanical flexibility,

---

[1] School of Energy and Chemical Engineering, Ulsan National Institute of Science and Technology (UNIST), Ulsan Metropolitan City, Republic of Korea. [2] These authors contributed equally: Yoojin Chang, Sangyun Na, Yun Goo Ro. ✉e-mail: hyunhko@unist.ac.kr

inherent ion conductivity[5], and biodegradability, making them suitable for wearable[6] and implantable[7] applications. However, their widespread implementation remains limited by issues such as environmental instability[8], limited ion-trapping capabilities, and high energy consumption. Overcoming these limitations is essential to realize low-power, bioresorbable neuromorphic systems capable of reproducing key neural processes such as PSC regulation, STP/LTP transitions, and bidirectional PPF/PPD modulation.

To achieve such functionalities, biopolymer-based artificial synapses have been realized using transistor-type and two-terminal configurations, which regulate ion migration and accumulation through electric field stimuli. While three-terminal transistors emulate biological synapse structures via electrolyte-gated channels[9,10], they typically require non-biodegradable electrodes[11–13] and suffer from high energy consumption due to gate bias operation. Alternatively, two-terminal devices, such as memristors based on metallic resistive layers or polymer-based architectures[14], offer structural simplicity and inherently low power consumption[15] by regulating ion flux within a single active layer[7,16]. However, most biodegradable memristors still rely on non-degradable redox-active electrodes such as silver (Ag), gold (Au), and indium tin oxide (ITO). Furthermore, their operation often involves unstable ionic filament formation, which causes abrupt conductance changes and necessitates high voltage inputs[17]. Additionally, polymer-based artificial synapses often lack sufficient ion-trapping sites[14], limiting long-term reliability. Efforts to address these limitations include the use of redox-active biodegradable electrodes such as magnesium (Mg)[7,16,18] and the incorporation of defect-rich sites[7,19]. However, these approaches often compromise energy efficiency and long-term stability. Therefore, a critical need remains for fully biodegradable artificial synapses that combine robust mechanical stability, energy-efficient operation, and reproducible synaptic functionality.

Herein, we report a fully biodegradable multilayer artificial synapse (M-AS) with a vertically stacked configuration of crosslinked chitosan–guar gum (CS–GG) ion-active layers (IALs) and a cellulose acetate (CA) ion-binding layer (IBL) (Fig. 1a). The trilayer configuration facilitates interfacial ion trapping via ion–dipole coupling (IDC) while achieving mechanical and environmental stability through hydrogen-bonded crosslinking within the CS–GG matrix. This architecture supports diverse synaptic functions, including bidirectional PSC modulation, PPF, STP, and LTP, with multilevel plasticity states that are tunable by both voltage amplitude and pulse number. In addition, the M-AS achieves an ultra-low energy consumption of 0.85 fJ per synaptic event —lower than that of biological synapses—and the longest reported long-term memory time of 5944 s among biodegradable artificial synapses. As a proof-of-concept application, the M-AS is integrated with a thermistor and robotic actuator to demonstrate a bioinspired reflexive system capable of stimulus-based learning, risk recognition, and reflex-like behavior.

Biomimetic device architecture and operating mechanism

The M-AS was structurally and functionally inspired by biological synapses (Fig. 1b). In biological systems, presynaptic stimulation releases neurotransmitters into the synaptic cleft, where they bind to receptors on the postsynaptic neuron and trigger the opening of ion channels, thereby leading to signal transmission and synaptic plasticity (Supplementary Fig. 1). Mimicking this structure and function, the M-AS consists of a biomimetic trilayer structure comprising an IBL sandwiched between two IALs, with vertically stacked biodegradable Mg electrodes (Fig. 1a). The IALs are composed of polysaccharide-based biopolymers, chitosan (CS) and guar gum (GG), extracted from crab shells and guar beans, respectively (Fig. 1ai). These biopolymers are crosslinked via hydrogen bonding to enhance mechanical integrity and moisture resistance. Sodium chloride (NaCl) is incorporated into the IALs as a neurotransmitter analog to facilitate ion transport and accumulation, analogous to processes in a biological synapse. Its high mobility promotes low-energy ion migration compared to larger ions such as bis(trifluoromethanesulfonyl)imide[20] and lithium perchlorate[21]. The IBL, composed of dielectric cellulose acetate (CA), acts as a postsynaptic receptor (Fig. 1aii). It provides dipolar sites for ion-dipole coupling (IDC) at the IAL–IBL interface, supporting efficient ion accumulation to facilitate synaptic behaviors including PSC, PPF, PPD, STP, and LTP. The top and bottom electrodes, made of biodegradable Mg electrodes, emulate neural axons and serve as a signal pathway.

Mimicking the biological synaptic process with ion transportation across the synaptic cleft (Fig. 1bi) and ion accumulation within the postsynaptic neuron (Fig. 1bii), M-AS provides a conceptual analogy to the synaptic behavior of a biological synapse. Under resting conditions, ions within the IALs remain randomly distributed, similar to neurotransmitters prior to synaptic release. Upon voltage application to the top electrode—analogous to presynaptic stimuli—ions migrate toward the IAL–IBL interface (Fig. 1ci), emulating neurotransmitter transport. Following the stimulus, some ions return to their original positions, while others are retained at the interface via IDC (Fig. 1cii), generating an asymmetric current profile (Supplementary Fig. 2). This partial ion retention, quantitatively determined to be 71.4% (Supplementary Fig. 3), leads to a gradual enhancement of PSC under repeated stimulation, analogous to the cascade-like biological signal transduction[22]. As a result, ion doping from the pristine polymer matrix enables low energy consumption, even lower than that of biological synaptic energy[2,15]. In addition, the introduction of IBL enhances localized ion accumulation and long-term memory (LTM) time, defined as the decay period until the current returns to its pre-stimulation value (Fig. 1d). The sequentially stacked IAL–IBL configuration further extends LTM time by increasing the number of ion storage sites and reinforcing IDC interactions.

Robust and biodegradable biopolymer network via hydrogen bonding

Polysaccharide-based biopolymers such as cellulose[23], chitosan[24], and carrageenan[5] have been widely utilized in biodegradable electronics owing to their flexibility and ease of processing[25,26]. However, their hydrophilic nature and thermodynamic instability[27] reduce durability in humid and high-temperature environments, limiting long-term device applicability. To enhance stability, we developed a crosslinked CS–GG biopolymer, forming a robust double-network structure through hydrogen bonding (H-bonding)[25]. CS and GG are abundant, low-cost natural polymers with amino ($-NH_2$) and hydroxyl ($-OH$) groups that promote polymer-ion interactions. Both have been reported to be biocompatible with low cytotoxicity[28,29]. The double network forms via pH-induced neutralization of CS, which promotes aggregation and crosslinking with GG, improving thermal and moisture resistance[30]. Specifically, neutralization converts $-NH_3^+$ groups in CS to $-NH_2$ (Supplementary Fig. 4), weakening electrostatic stabilization. These neutralized CS chains are further stabilized through intermolecular H-bonding with $-OH$ groups in GG[25,26] (Fig. 2a).

Fourier-transform infrared (FT-IR) confirmed successful crosslinking by showing suppressed intramolecular vibrations and enhanced intermolecular H-bonding signatures, indicating strong CS–GG interactions (Supplementary Fig. 5a, b and Supplementary Note 1). This H-bonded network significantly improved the environmental and mechanical stability of IAL. Density functional theory (DFT) calculations supported the enhanced stability of the crosslinked CS–GG network, revealing stronger H-bonding interactions compared to non-crosslinked counterparts (Supplementary Fig. 6). Consistent with DFT results, the crosslinked film maintained structural integrity in phosphate-buffered saline (PBS, pH ≈ 7.4) for over 24 hours (Fig. 2bi), whereas the non-crosslinked counterpart swelled into a mechanically

https://doi.org/10.1038/s41467-025-66511-3

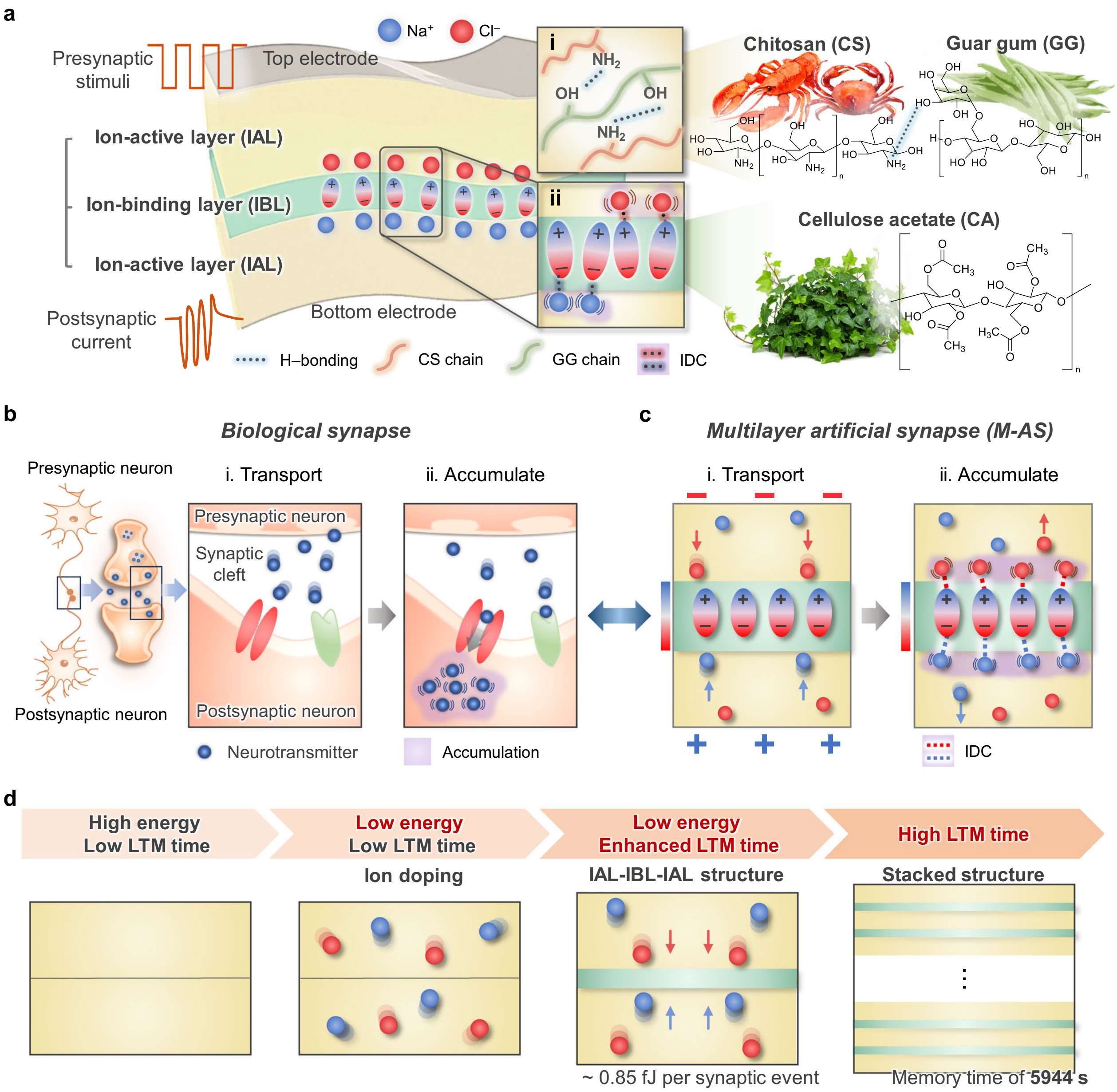

Fig. 1 | Concept of the biodegradable multilayer artificial synapse. a Schematic of the M-AS with an IAL–IBL–IAL multilayer configuration: (i) crosslinked CS–GG IALs via hydrogen bonding between –OH and –NH_2 groups of CS and GG, and (ii) IDC at the IAL–IBL interface. **b** Schematic illustration for the working mechanism of a biological synapse: (i) neurotransmitter transport under presynaptic stimuli and (ii) ion accumulation inside the postsynaptic neuron. **c** Working mechanism of the M-AS: (i) ion transport under a presynaptic voltage pulse, and (ii) ion accumulation via IDC after stimulus. **d** Design strategies for achieving low energy consumption and long LTM time in the artificial synapse: ion doping, incorporation of an IBL, and multilayer stacking of IAL–IBL layers for extended LTM.

weak hydrogel (Fig. 2bii). It also suppressed moisture-induced swelling, showing a nearly 12-fold lower water uptake than the non-crosslinked film (Supplementary Fig. 7a), particularly at 60 wt% CS (Supplementary Fig. 7b).

Thermogravimetric analysis (TGA) revealed reduced water-induced weight loss and a higher thermal degradation temperature for the crosslinked CS–GG, indicating enhanced thermal stability (Supplementary Fig. 8a–c and Supplementary Note 2). While the non-crosslinked film exhibited a dramatic humidity dependence with a 9.5-fold increase in elongation at break due to water-induced plasticization and loss of structural integrity, the crosslinked film maintained stable performance (Fig. 2c). The crosslinked CS–GG network also exhibited excellent mechanical durability under repeated folding and crumpling in both ambient and PBS conditions (Supplementary Fig. 9). Furthermore, biodegradability was confirmed through a soil burial test, in which the complete decomposition of the M-AS, composed of multilayer IALs (crosslinked CS–GG) and a cellulose-based IBL with Mg electrodes, occurred within 16 days. This decomposition was facilitated by microbial and fungal activity in water-containing soil (Fig. 2d), and was accompanied by a gradual weight decrease (Supplementary Fig. 10a). To further verify decomposition, FT-IR analysis at different burial stages showed a progressive reduction of characteristic functional groups of CS and GG (Supplementary Fig. 10b). Additionally, XRD analysis revealed broadening and reduction in intensity of the 20.1° peak, indicating the gradual loss of crystallinity in the crosslinked polymer network. (Supplementary Fig. 10c). Finally, the pH of the surrounding soil remained stable throughout the degradation period (Supplementary Fig. 10d), highlighting the eco-friendly and transient nature of the device without adverse byproduct effects.

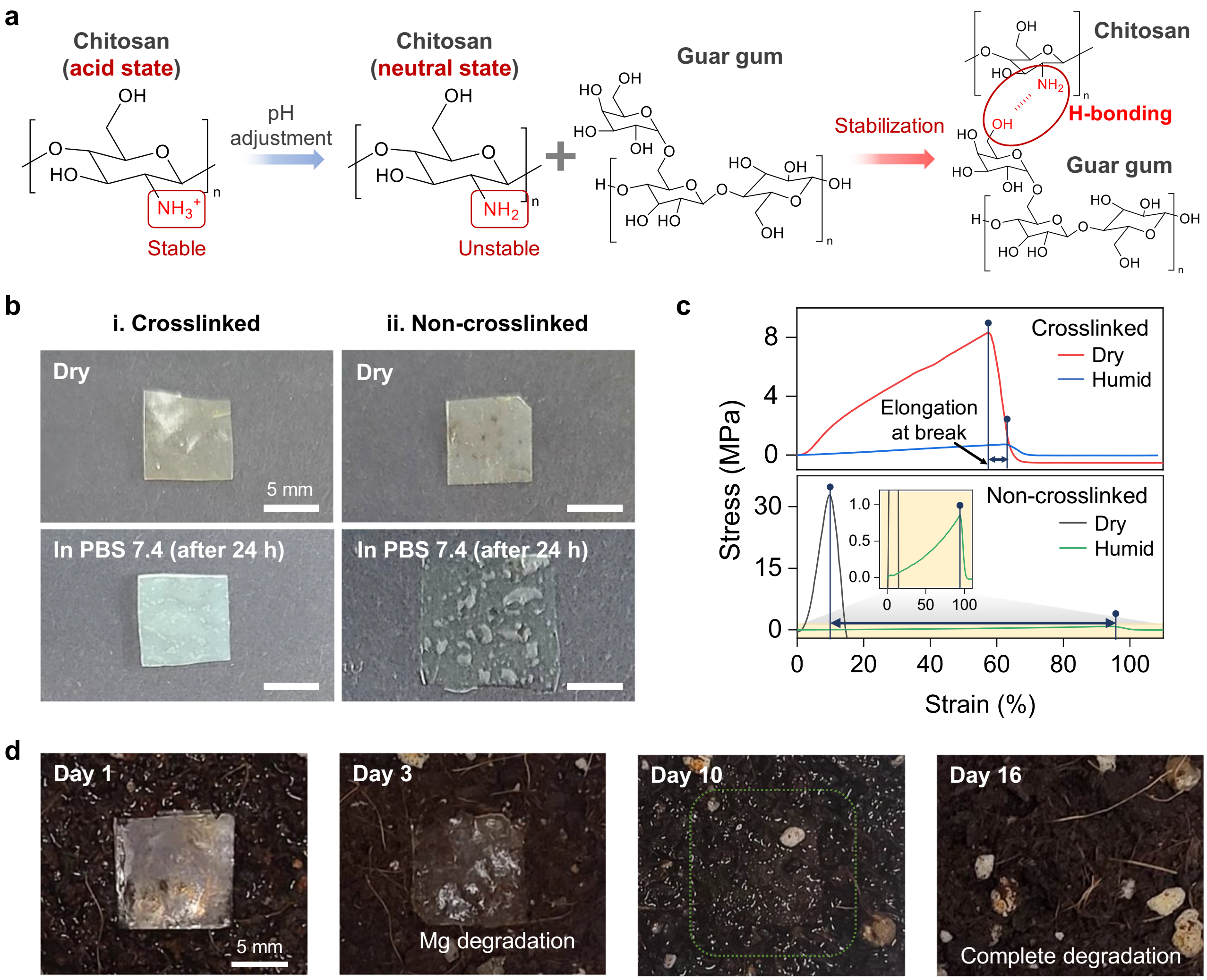

Fig. 2 | Characterization of the robust and biodegradable CS–GG biopolymer matrix. a Hydrogen-bonded crosslinking mechanism between CS and GG. **b** Photographs of CS–GG films under dry conditions and after immersion in PBS (pH 7.4, 24 h): (i) crosslinked and (ii) non-crosslinked samples. The reduced transparency of the films after PBS immersion is due to increased porosity with slight swelling. **c** Stress–strain curves of crosslinked (red, blue) and non-crosslinked (black, green) CS–GG under dry and humid conditions. The crosslinked sample exhibits stable elongation at break values (57.6% dry, 64.2% humid), while the non-crosslinked sample shows a dramatic humidity-dependent increase from 10.1% (dry) to 95.2% (humid) due to water-induced plasticization. **d** Sequential images showing the time-dependent biodegradation process of the M-AS in a natural soil environment over 16 days.

Ion retention enabled by IDC at the IAL–IBL interface

To emulate synaptic functionality, we designed an M-AS with a trilayer configuration that reflects neural synapses (fabrication processes in Supplementary Fig. 11), evaluating ionic response under electrical stimulation. Under an applied voltage, Na$^+$ and Cl$^-$ ions migrate through the IALs and accumulate at the IAL–IBL interface via IDC. Importantly, a portion of the ions is retained at the interface even after stimulus removal, resulting in asymmetric PSC responses. With repeated stimuli, the progressive ion accumulation enhances the PSC in a stepwise manner, effectively reproducing synaptic potentiation and LTP.

As a control, we fabricated an IAL–IAL device without an intermediate IBL (Supplementary Fig. 12a). Upon voltage application, the device exhibited symmetric PSCs during and after the pulse (Fig. 3a and Supplementary Fig. 13a), indicating negligible ion retention. Repeated stimulation produced constant PSCs without potentiation (Fig. 3b). Electrochemical impedance spectroscopy (EIS) analysis revealed a Nyquist plot with a single semicircle and a spike (Fig. 3c). The semicircle corresponds to the intrinsic resistance-capacitance (RC) response of the IAL and electric double layer (EDL) formation at the IAL-electrode interface, respectively. The single semicircle indicates the absence of an interfacial layer that could promote ion accumulation via IDC. Consequently, oppositely charged ions freely diffuse after stimulation, leading to minimal interfacial ion trapping (Supplementary Fig. 13b)[31]. Cyclic voltammetry further confirmed the absence of ion adsorption or redox reactions within ±1 mV (Supplementary Fig. 14a–b). These results collectively indicate that without an IBL, the EDL alone cannot sustain charge separation after the pulse[32], thereby precluding ion retention and synaptic behavior. The limited role of the EDL at the metal-IAL interface was further examined using an IAL-metal-IAL structure with a platinum (Pt) interlayer to induce EDL formation at IAL–Pt interfaces (Fig. 3d). Similar to the IAL–IAL, this structure exhibited symmetric PSCs, indicating no potentiation (Fig. 3e). EIS analysis revealed a nearly identical Nyquist plot with a single semicircle and a spike (Fig. 3f). These results confirm that the introduction of a metal interlayer does not promote ion accumulation at the interface, and that EDL formation alone, without an IBL, is insufficient to induce synaptic behavior. Therefore, in both IAL–IAL structures, with and without a metal interlayer, ion diffusion occurs without retention, resulting in the preclusion of synaptic potentiation.

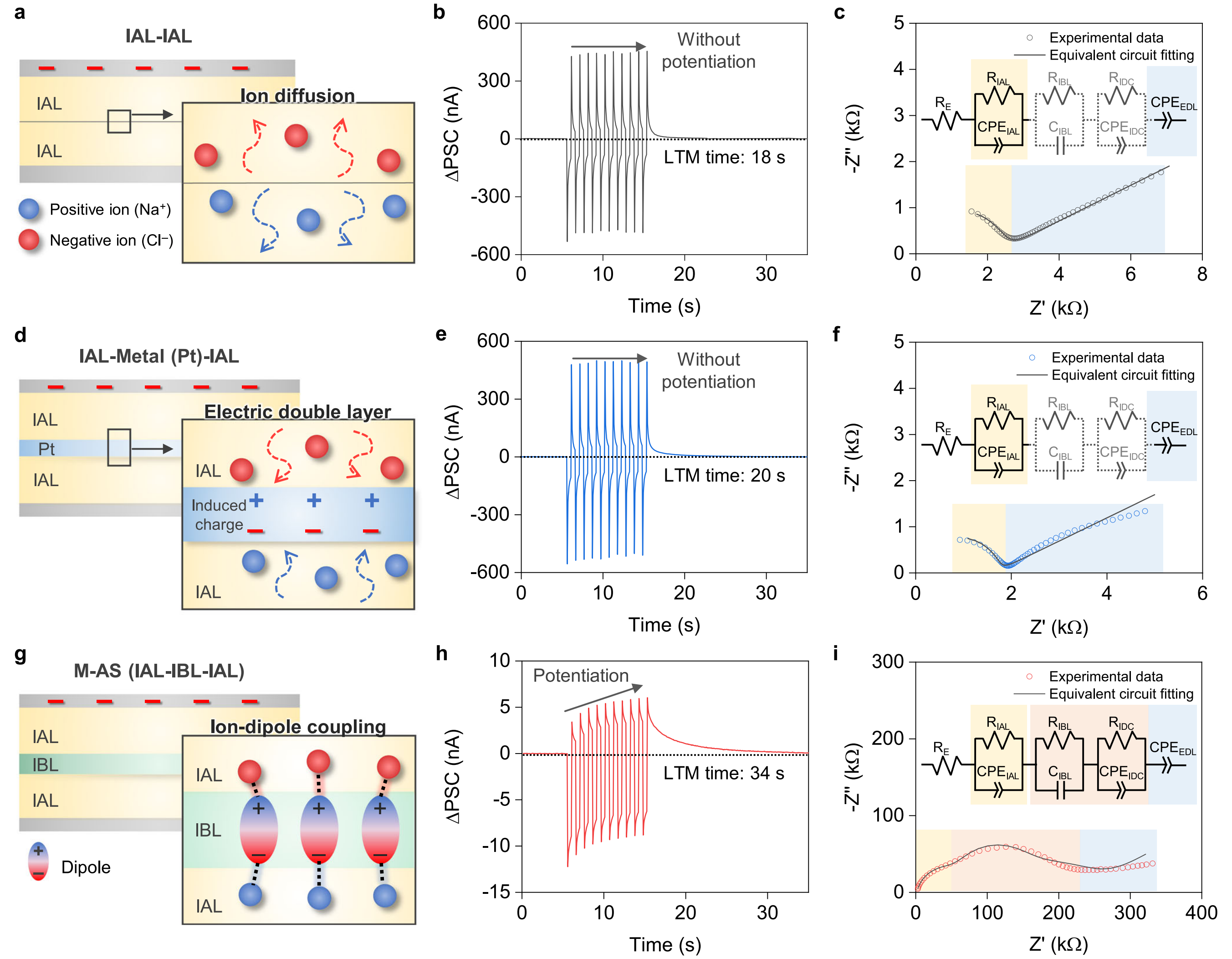

Fig. 3 | Synaptic behavior and ion dynamics of the M-AS. a Schematic of the M-AS with an IAL–IAL configuration lacking an IBL. **b** PSC response of the IAL–IAL structure under repeated voltage pulses (−1 mV, 0.5 s pulse width, and 1 Hz for 10 pulses), showing symmetric currents due to negligible ion accumulation. **c** Nyquist plot of the IAL–IAL device showing IAL resistance and EDL capacitance (Inset: equivalent RC circuit with IAL and EDL). **d** Schematic of the M-AS with an IAL–Pt–IAL structure to evaluate the effect of metal interfaces. **e** PSC response of the IAL–Pt–IAL structure under repeated voltage pulses (−1 mV, 0.5 s pulse width, and 1 Hz for 10 pulses), showing symmetric behavior. **f** Nyquist plot of the IAL–Pt–IAL device showing IAL resistance and EDL capacitance (Inset: equivalent RC circuit with IAL and EDL). **g** Schematic of the M-AS with an IAL–IBL–IAL configuration showing IDC formation at the IAL–IBL interface. **h** PSC response of the IAL–IBL–IAL structure under repeated voltage pulses (−1 mV, 0.5 s pulse width, and 1 Hz for 10 pulses), exhibiting asymmetry due to ion accumulation. **i** Nyquist plot of the IAL–IBL–IAL device showing two distinct semicircles corresponding to EDL and IDC capacitances (Inset: equivalent RC circuit with IAL, IBL, IDC, and EDL).

To enable ion retention, an IBL was introduced between the IALs (scanning electron microscopy (SEM) image in Supplementary Fig. 12b) to facilitate ion-dipole interactions. CA, a biodegradable and biocompatible dielectric material[33,34], was selected as the IBL due to its ability to align dipoles under an applied voltage. Voltage application drives ion migration within the IALs and dipole alignment in the IBL, inducing IDC at the IAL–IBL interface (Fig. 3g)[35]. Unlike the EDL, which requires a continuous bias, IDC arises from electrostatic interactions between ions and aligned dipoles and persists even after stimulus removal. This delayed ion return produces asymmetric PSCs with reduced reverse current (Supplementary Fig. 13c–d). This IDC-enabled mechanism allows the M-AS to exhibit key synaptic behaviors, including PSC potentiation and LTP under repeated voltage pulses (Fig. 3h). To quantitatively demonstrate the presence of IDC capacitance in the IAL–IBL–IAL structure, EIS analysis was performed, which reveals two distinct semicircles in the Nyquist plot (Fig. 3i), corresponding to the IAL resistance and the interfacial IDC capacitance, respectively (Supplementary Table 1). The equivalent circuit fitting confirmed that IDC capacitance appears only in the IAL-IBL-IAL structure, verifying ion accumulation at the IAL-IBL interface and supporting the IDC mechanism. Finite element analysis (FEA) further demonstrated the role of IBL incorporation (Supplementary Note 3): in the IAL-IAL structure (Supplementary Fig. 15ai, 15bi), the electric potential is broadly distributed, and the electric field remains uniformly across the device. In contrast, M-AS exhibits localized potential concentration across the IAL–IBL interface (Supplementary Fig. 15aii, 15bii), leading to a distinct interfacial potential distribution and a pronounced potential drop at the IAL-IBL interface. This concentrated field facilitates stronger dipole alignment and supports the proposed IDC mechanism. To further evaluate the impact of IDC, we applied varying numbers of pre-pulses before EIS analysis (Supplementary Fig. 16a). As the pulse number increased, the semicircle diameter expanded, indicating greater interfacial resistance due to progressive ion trapping and reduced mobile ion concentration (Supplementary Fig. 16b, Supplementary Table 2). Moreover, to complement the electrical results, we performed energy dispersive spectroscopy (EDS)

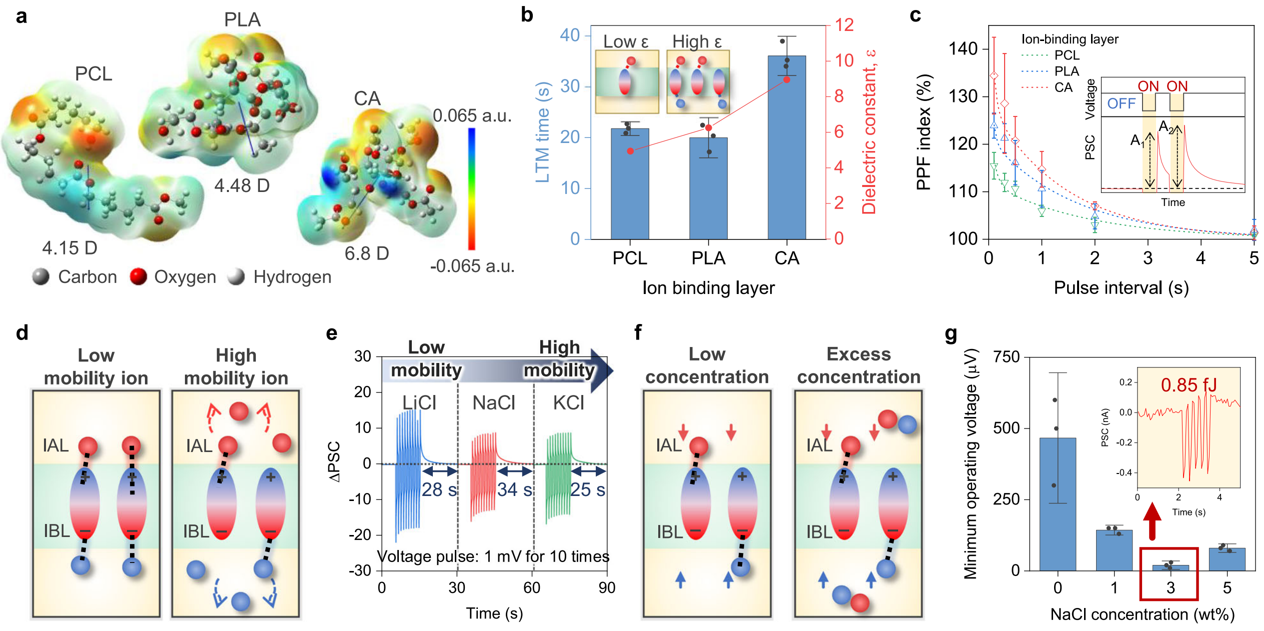

Fig. 4 | Optimization of IBL materials and ion properties for energy-efficient synaptic performance. a DFT-calculated molecular dipole moments and electrostatic potential maps of biodegradable dielectrics (PCL, PLA, and CA) used as IBLs. Electrostatic potential maps exhibit red and blue regions representing areas of more negative and positive charges, respectively. **b** Comparison of LTM time (−1 mV, 1 Hz, 10 pulses) and dielectric constant (measured at 100 Hz) for M-ASs incorporating different IBLs. **c** PPF index of M-ASs with different IBLs as a function of pulse interval (inset: PSC responses under two consecutive pulses (−1 mV) for PPF index calculations). Error bars in (**b**) and (**c**) denote standard deviation from three different samples. **d** Schematic illustrating the effect of ion mobility on ion diffusion behavior following a voltage pulse. **e** PSC responses of M-ASs with different ion species (3 wt% LiCl, NaCl, and KCl) under 10 repetitive pulses at −1 mV (0.5 s pulse width, and 1 Hz for 10 pulses under 45% RH). **f** Schematic depicting ion migration depending on ion concentration. **g** Minimum operating voltage of M-ASs as a function of NaCl concentration, with 3 wt% as the optimal condition. (Inset: PSC response achieved with the lowest operating voltage (−20 μV) with energy consumption of 0.85 fJ).

of the M-AS after electrical stimulation at −0.8 V and 15 min relaxation (Supplementary Fig. 17). The results show a uniform Na^+ distribution without electrical stimulation and localized Na^+ accumulation at the bottom IAL–IBL interface after applying electrical stimulation, consistent with IDC-driven ion accumulation. These results demonstrate that the IBL facilitates effective ion retention through IDC, enabling synaptic potentiation and improved plasticity in the M-AS.

Optimization of IBL and ion parameters for synaptic efficiency

To emulate biological synapses with low energy consumption, it is crucial to regulate neurotransmitter-like ion migration and accumulation precisely. Achieving such energy efficiency requires IBLs with high dielectric constants for strong dipole alignment and ions with appropriate mobility for controlled ion diffusion and accumulation via IDC. For various biodegradable IBL candidates including polycaprolactone (PCL), polylactic acid (PLA), and CA (Supplementary Fig. 18), we performed DFT to determine molecular dipole moments and electrostatic potential maps for enhanced IDC via dipole alignment (Fig. 4a). CA exhibited the highest dipole moment due to its abundant polar functional groups[36], with distinct electrostatic regions favoring interaction with Na^+ and Cl^-, making it favorable for IDC formation. The calculated dipole moments closely matched with experimentally measured dielectric constants, with CA exhibiting the highest value (Fig. 4b). To further elucidate the interactions between biodegradable IBLs and Na^+/Cl^- ions, interaction energies were calculated using DFT (Supplementary Fig. 19). CA exhibits the highest interaction energy with both ions compared to the other IBLs (PCL and PLA), highlighting the enhanced IDC in CA. Consequently, M-AS employing CA as the IBL demonstrated superior synaptic performance, including the longest LTM time (36 s) among biodegradable candidates. While fluoropolymers like polyvinylidene fluoride-trifluoroethylene (P(VDF-TrFE)) exhibited even longer LTM time (40 s) due to their outstanding dielectric properties (Supplementary Fig. 20), their poor biodegradability and potential toxicity limit their applicability. Consequently, CA was selected as the optimal IBL material, offering a favorable balance of biodegradability, biocompatibility, and synaptic performance.

In addition to LTP, STP, retaining stimuli for less than 30 seconds[37], was evaluated using the PPF index. This index quantifies the relative enhancement of the second PSC (A_2) compared to the first (A_1), calculated as

$$\text{PPF index } (\%) = (A_2/A_1) \times 100 \tag{1}$$

A higher PPF index reflects stronger facilitation, indicating the ability of the synaptic interface to retain ionic perturbations from the initial stimulus and amplify the response to subsequent inputs. At a pulse interval of 0.1 s, the PPF index was highest with CA as the IBL, followed by PLA and PCL, demonstrating superior STP with CA (Fig. 4c). To analyze temporal characteristics, the PPF values across different pulse intervals were fitted using a double-exponential decay,

$$y = 1 + C_1 \times \exp(-t/\tau_1) + C_2 \times \exp(-t/\tau_2), \tag{2}$$

where C_1 and C_2 are fitting coefficients, t is the pulse interval, and τ_1 and τ_2 represent the fast and slow relaxation times, respectively. In biological synapses, τ_1 and τ_2 typically correspond to 40 ms and 300 ms, respectively[38], indicating how quickly synaptic potentiation decays. Notably, M-ASs with an IBL exhibited relaxation times closer to biological values than those with IAL–IAL configurations (Supplementary Fig. 21 and Supplementary Table 3), suggesting that dipole-aligned interfaces effectively preserve transient ionic states. The combination of a high PPF index and biologically matched relaxation times implies that the CA-based M-ASs achieve both enhanced synaptic responsiveness and appropriate temporal resolution.

Ion mobility within the IAL significantly influences the energy efficiency of synaptic behavior. High-mobility ions facilitate rapid ion migration[39,40], lowering the operating voltage and energy consumption. However, excessive mobility can lead to back-diffusion after stimulation, weakening IDC and reducing net ion accumulation at the interface (Fig. 4d). To investigate this trade-off, we compared the LTM time of M-AS devices using LiCl, NaCl, and KCl under identical stimulation conditions (Fig. 4e). Interestingly, the Na^+-containing M-AS exhibited the longest LTM time, followed by Li^+ and K^+, despite the latter having higher intrinsic ion mobilities ($Li^+ < Na^+ < K^+$, Supplementary Table 4). The superior performance of Na^+ is attributed to its balanced mobility and lower hygroscopicity compared to Li^+. LiCl exhibits strong moisture absorption[41], which facilitates ion dissociation under humid conditions, enhancing ionic conductivity but causing instability. As a result, LiCl-containing devices exhibited greater PSC variation with humidity (Supplementary Fig. 22a), while NaCl-containing devices remained stable (Supplementary Fig. 22b), resulting in superior memory performance. Nyquist plots supported these trends: LiCl-containing M-AS showed reduced IAL resistance and IDC capacitance due to moisture-enhanced ion conductivity (Supplementary Fig. 23a–c), while KCl-containing M-AS exhibited low IDC capacitance owing to its high ion mobility (Supplementary Table 5), limiting ion accumulation. These findings suggest that Na^+ provides an optimal balance between ion mobility and hygroscopicity, enabling enhanced interfacial ion retention, improved synaptic performance, and stable operation under varying humidity.

Beyond ion species, ion concentration within the IAL critically affects the operating voltage and, consequently, energy consumption. As shown in Fig. 4f, low concentrations provide insufficient mobile ions for effective synaptic operation. In contrast, excessive concentrations induce ionic crowding, reducing mobility and hindering efficient migration[42], ultimately increasing the operating voltage. We evaluated the minimum operating voltage at varying NaCl concentration and found that 3 wt% NaCl sample yielded the lowest value of −20 μV, corresponding to an exceptionally low energy consumption of 0.85 fJ per synaptic event (Fig. 4g). This value is significantly lower than that of biological synapses (1–10 fJ per synaptic event)[43]. The energy consumption was calculated as

$$E = I \times V \times t, \tag{3}$$

where I is the PSC, V is the minimum operating voltage for synaptic behavior, and t is the pulse interval. Moreover, to confirm the peak signals at −20 μV, signal-to-noise ratio (SNR) analysis was performed, revealing that PSCs originate from true device responses rather than instrumental noise (Supplementary Fig. 24, Supplementary Note 4). Furthermore, activation energy analysis under varying humidity conditions showed that water-assisted ion migration reduces the energy barrier, enabling ionic motion at ultra-low voltages, consistent with the observed PSCs and synaptic performance (Supplementary Fig. 25, Supplementary Note 5). These results highlight the importance of balancing ion mobility and concentration to achieve energy-efficient synaptic performance. The optimized M-AS (CA as the IBL and 3 wt% NaCl in the IAL) consistently demonstrated both STP and LTP, closely emulating biological synapse functions. Unless otherwise stated, this optimized M-AS configuration was employed for all subsequent experiments. For practical applicability, M-AS not only reproduces biological functions but also sustains reliable operation. Owing to crosslinked CS–GG and IDC, the optimized M-AS maintains stable synaptic behaviors under repeated stimulation, varying humidity, and mechanical stress (Supplementary Fig. 26, Supplementary Note 6). These features highlight the feasibility of M-AS, which combines biological fidelity with long-term stability, environmental stability with encapsulation, and mechanical durability.

Voltage-tunable synaptic plasticity and multilevel memory encoding

In a biological synapse, excitatory and inhibitory postsynaptic currents (EPSCs and IPSCs) are generated through ion influx and efflux across the postsynaptic membrane in response to presynaptic stimulation. EPSCs result from cation influx (e.g., Na^+, Ca^{2+}), while IPSCs arise via anion influx (e.g., Cl^-) or cation efflux (e.g., K^+) (Supplementary Fig. 27a–b). These bidirectional ionic flows regulate membrane potential—depolarization for EPSC and hyperpolarization for IPSC—modulating synaptic plasticity and enabling learning and memory[39,40]. Similarly, our M-AS exhibits polarity-dependent PSCs that emulate both EPSC- and IPSC-like behaviors. A negative voltage pulse (−1 mV, 1 Hz) induces a positive PSC (excitatory), while a positive pulse (1 mV, 1 Hz) produces a negative PSC (inhibitory) (Fig. 5a and Supplementary Fig. 27c, d). Furthermore, the PSC amplitude scales proportionally with the input voltage magnitude in both polarities (Fig. 5b), indicating directional and amplitude-dependent ion migration within the IALs. Notably, the M-AS responds distinctly even under ultra-low voltages down to 0.1 mV. This voltage-dependent bidirectionality allows the M-AS to mimic key functionalities of biological synapses, including bidirectional excitatory/inhibitory signal modulation and graded synaptic strength based on input magnitude.

Beyond polarity-dependent responses, the synaptic strength of the M-AS can also be modulated quantitatively by tuning electrical stimulation parameters such as pulse width, amplitude, and number. As shown in Fig. 5c, PSC is enhanced as the pulse width increases while the amplitude remains constant, which is attributed to the extended ion migration within the IALs. Additionally, in Fig. 5d, the PSC magnitude increases with voltage amplitude (Supplementary Fig. 28a) and the LTM time can be modulated by voltage amplitude (Supplementary Fig. 28b), ranging from 22 s at −0.1 mV to 635 s at −1 V (10 pulses, Supplementary Fig. 29). This voltage-dependent plasticity closely resembles biological synapses, where synaptic strength is modulated by spike amplitude[44,45]. Furthermore, the LTM time is proportional to the number of input pulses, emulating memory reinforcement through repetitive stimulation (Fig. 5e and Supplementary Fig. 28c)[45,46]. Together, these results demonstrate that the M-AS enables multilevel plasticity, with memory strength adjustable through either pulse amplitude or number. In addition, the device supports bidirectional synaptic modulation, achieving both excitatory and inhibitory potentiation depending on the polarity of the input voltage[47].

Due to its multilevel plasticity, the M-AS supports a learning-forgetting-relearning process, where repeated learning stimulation progressively enhances LTM time beyond 200 s (Fig. 5f). This multilevel plasticity allows the M-AS to encode both the history and intensity of repeated stimuli through cumulative synaptic strengthening. This property facilitates both memory reinforcement and recovery from intermediate forgetting. As a result, cyclic stimulation induces a transition from STP to LTP, even with intermediate forgetting between learning cycles. Notably, the LTM time can reappear through a relearning process even after complete forgetting in cycle tests (Supplementary Fig. 30). Such behavior closely resembles biological learning, where repeated exposure to stimuli strengthens synaptic connections[48].

In contrast to previous biodegradable artificial synapses with memristor structures, which rely on non-biodegradable electrodes for redox reactions, our M-AS utilizes fully biodegradable electrodes and active layers. Existing fully biodegradable synapses typically require high operating voltages (1 V) to induce PSCs via interfacial ion

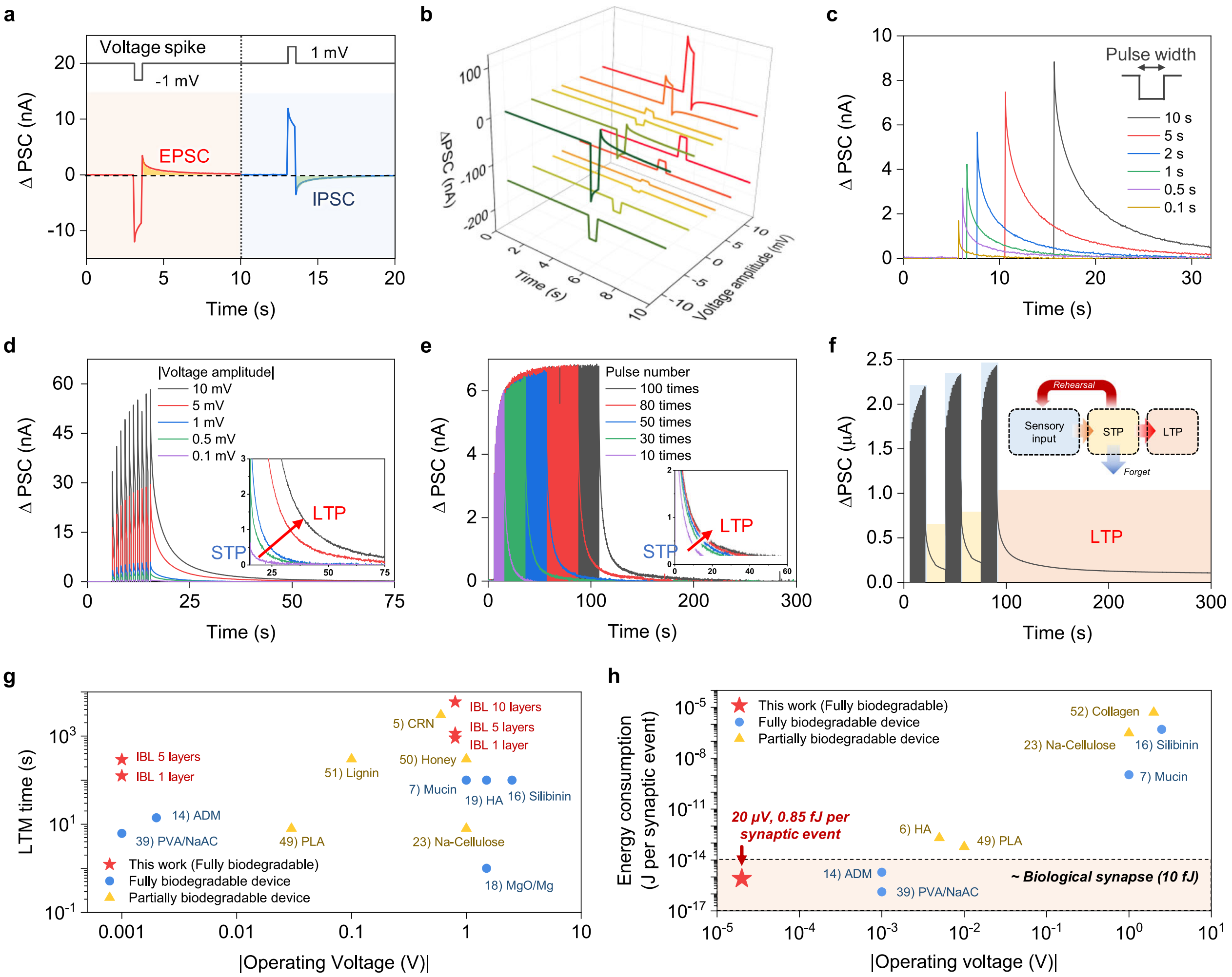

Fig. 5 | Energy-efficient synaptic performance and multilevel plasticity in the M-AS. a PSC responses under negative and positive voltage pulses, mimicking EPSC and IPSC, respectively. **b** PSC amplitude as a function of input voltage magnitude and polarity, showing proportional and bidirectional ion migration, even at ultra-low voltages (1–10 mV). **c** PSC responses as a function of pulse width at constant voltage (−1 mV), demonstrating enhanced ion migration with longer pulse duration. **d** Transition of synaptic plasticity from STP to LTP as a function of voltage amplitude (− 0.1 to −10 mV, 10 pulses at 0.5 s pulse width), demonstrating voltage-tunable plasticity states. **e** Transition of synaptic plasticity from STP to LTP with increasing pulse number (−1 mV, 0.5 s pulse width), showing memory strengthening via repetitive stimulation. **f** Learning-forgetting-relearning behavior for synaptic plasticity transition under cyclic pulse application (− 500 mV, 15 pulses per cycle), demonstrating gradual memory reinforcement and transition from STP to LTP. Blue, yellow, and red boxes indicate learning, forgetting, and LTP phases, respectively. Inset: schematic illustration of biological STP-to-LTP transition for conceptual comparison. **g** Comparison of LTM retention time versus operating voltage between M-AS and previously reported two-terminal biodegradable artificial synapses. **h** Comparison of operating voltage and energy consumption among the M-AS, previously reported two-terminal biodegradable artificial synapses, and biological synapses, highlighting the superior energy efficiency of the M-AS.

accumulation or redox reactions at electrodes (Supplementary Fig. 31). While partially biodegradable devices with inert metal electrodes can operate at lower voltages, they compromise environmental compatibility. Notably, the M-AS demonstrates LTP with an LTM time of 125 s at an ultralow voltage of 1 mV (Supplementary Fig. 32a), which is the longest reported among fully biodegradable synapses (Supplementary Table 6), even outperforming partially biodegradable counterparts at the same voltage. Increasing the voltage to 0.8 V further extends the LTM time to 904 s (Supplementary Fig. 32b), attributed to enhanced ion accumulation at the IAL–IBL interface (Fig. 5g)[5,7,14,16,18,19,23,39,49–51]. Remarkably, stacking additional IAL–IBL layers linearly increases the number of ion accumulation sites, extending LTM time up to 5944 s with a 10-layer configuration (Supplementary Fig. 33a–c). This value represents the longest LTM time among biodegradable artificial synapses, including both transistor- and two-terminal-based architectures (Supplementary Fig. 34a, Supplementary Table 7). Notably, it is also comparable to non-biodegradable artificial synapses, which typically exhibit similar LTM times but only under relatively high operating voltages (> 0.1 V) (Supplementary Tables 8 and 9, Supplementary Fig. 35a). When compared with two-terminal (Fig. 5, Supplementary Table 10)[6,7,14,16,23,39,49,52] and transistor-based (Supplementary Fig. 34b and Supplementary Table 11) biodegradable artificial synapses, the M-AS also operates at significantly lower voltage and energy consumption, even surpassing biological synapses in energy efficiency. Furthermore, although fully biodegradable, the M-AS demonstrates energy consumption comparable to that of state-of-the-art non-biodegradable synapses (Supplementary Tables 12 and 13, Supplementary Fig. 35b). These results underscore the M-AS as a promising platform for ultra-low-power and LTM time in biodegradable neuromorphic electronics.

Bioinspired reflexive system for thermal injury recognition

Humans respond to thermal injuries such as burns or frostbite through a multi-step biological process involving temperature detection, neural processing, and motor reflexes (Supplementary Fig. 36)[53]. To emulate this mechanism in robotics, we developed a bioinspired reflexive system consisting of a thermistor as a thermoreceptor, an M-AS as a synaptic processor, and robotic actuators that execute protective actions (Fig. 6a). In this system, the thermistor mounted on the palm of the robot (Fig. 6b) detects temperature changes and modulates its resistance, producing a temperature-dependent current (I_{Ther}) (Supplementary Fig. 37a). This current is converted into the presynaptic voltage pulse with a specific amplitude and polarity, which is then applied to the M-AS (Supplementary Fig. 37b). The resulting PSC from the M-AS activates a corresponding robotic response through signal-driven actuation (Fig. 6c, Supplementary Fig. 38). By leveraging the bidirectional response of the M-AS to presynaptic pulse polarity, the system distinguishes between thermal extremes: a negative pulse signifies a high-temperature (burn) stimulus, while a positive pulse indicates a low-temperature (frostbite) stimulus.

Unlike human neural adaptation, which can become desensitized to mild but continuous stimuli and delay protective action[54], the M-AS accumulates synaptic behaviors (e.g., PSC regulations, STP/LTP) through a learning process driven by repetitive low-level stimuli. This accumulation enables recognition of persistent thermal threats, promoting either LED signaling or object release. Once the PSC exceeds a predefined threshold, the system responds by illuminating LEDs to indicate danger and spreading the robotic fingers to drop the stimulus source. The number of illuminated LEDs reflects the injury severity, determined by the PSC magnitude. The duration of illumination reflects the LTP behavior of the M-AS, effectively representing a “healing time” after injury. This learning-based, reflex-like behavior illustrates how synaptic plasticity and polarity-sensitive signaling in the M-AS enable intelligent, adaptive behavior in artificial systems.

Within the safe temperature range, I_{Ther} remains below the activation threshold, thereby preventing presynaptic pulse generation and robotic response (Supplementary Fig. 39). To emulate a mild thermal injury scenario, known to cause protein damage after 10 s of contact with a 60 °C surface[55], the robotic hand was used to grasp a hand warmer. This action elevated I_{Ther} beyond the mild threshold, triggering a simulated mild burn via a low-amplitude presynaptic pulse. Because the thermal stimulus was subcritical, the system required prolonged input (over 40 s) to accumulate sufficient synaptic performance (Fig. 6di, ei). Under continuous stimulation, the PSC gradually increased and eventually exceeded the activation threshold (130 % of the initial value, Fig. 6dii), indicating significant synaptic potentiation. Then, the robotic hand opened to drop the hand warmer, while one red LED turned on, symbolizing a mild burn scar (Fig. 6eii). After release, I_{Ther} dropped below the threshold and the presynaptic pulse ceased. Meanwhile, the red LED remained lit over 400 s, reflecting the LTP behavior of the M-AS and representing the prolonged “healing time” during thermal recovery (Fig. 6diii, eiii and Supplementary Movie 1).

When exposed to extreme temperatures (>80 °C) capable of causing immediate skin damage, I_{Ther} rapidly surpasses the extreme threshold, generating a high-amplitude presynaptic pulse (Fig. 6f, Supplementary Movie 2). Before reaching this threshold, mild thermal stimulation causes I_{Ther} to surpass the mild threshold but below the extreme one, inducing only a small PSC (Fig. 6g). During this phase, insufficient synaptic learning prevents the PSC from exceeding the mild burn threshold, and no robotic response occurs. Once I_{Ther} crosses the extreme threshold, the PSC exceeds 500 nA, immediately triggering the robotic hand to release the heat source and illuminating all four red LEDs, indicating a severe burn. Following this protective action, I_{Ther} drops below the threshold, terminating the presynaptic pulse. LEDs remain illuminated for over 700 s, indicating the extended healing period required for recovery from severe thermal injury.

Conversely, under cold conditions that may cause frostbite, I_{Ther} drops below a defined cold threshold, generating a positive presynaptic pulse and inducing a PSC in the opposite direction to burn responses. To simulate mild frostbite, the robotic hand grasped an ice pack, triggering a low-amplitude pulse. After sufficient synaptic learning, this produced a moderate PSC that activated one green LED and caused the robotic hand to release the ice pack, signaling a mild frostbite event (Supplementary Fig. 40a–b). The LED remains illuminated for over 450 s as I_{Ther} gradually recovered, indicating thermal stabilization and recovery (Supplementary Movie 3). In contrast, exposure to extremely low temperatures, such as liquid nitrogen, immediately triggered a severe frostbite response (Supplementary Fig. 40c). Then, a high-amplitude presynaptic pulse generated a large PSC (over −500 nA), leading to rapid release of the ice and activation of all four green LEDs (Supplementary Movie 4). As in the extreme burn scenario, if I_{Ther} does not drop below the extreme cold threshold, the PSC from mild stimuli remains below the learning threshold, and no robotic response is triggered (Supplementary Fig. 40d). These results confirm that the M-AS enables multi-level thermal injury recognition based on both stimulus intensity and polarity, enabling human-like reflexive responses. With its capacity for continuous learning and adaptive behavior, this artificial reflexive system holds strong potential for integration into next-generation humanoid robots capable of real-time thermal perception and decision-making. Beyond thermal sensing, the same architecture can be extended to multimodal inputs through a single artificial synapse, providing a pathway toward more adaptive and context-aware robotic systems (Supplementary Fig. 41 and Supplementary Note 7).

Conclusions

In summary, we developed a fully biodegradable, robust, and energy-efficient artificial synapse featuring an IAL–IBL–IAL multilayer architecture composed of crosslinked CS–GG and CA. NaCl embedded in the ion-active layers serves as a mobile ionic species analogous to biological neurotransmitters. Upon electrical stimulation, ion migration and dipole alignment induce IDC at the IAL–IBL interface, enabling partial ion retention and cascade-like PSCs essential for memory formation. This mechanism supports key synaptic functionalities, including STP and LTP, bidirectional PSC modulation, and multilevel memory encoding. The M-AS achieves an ultra-low energy consumption of 0.85 fJ per synaptic event—lower than that of biological synapses—and exhibits the longest reported memory retention time (5944 s) among biodegradable artificial synapses, while maintaining mechanical integrity and environmental stability even under humid conditions. As a proof of concept, we integrated the M-AS into a bioinspired reflexive system that couples thermal sensing with reflex-like robotic actuation. This system discriminates between mild and severe thermal injuries and initiates appropriate reflex-like robotic actions. Importantly, it encodes both stimulus severity and recovery time via LTP-mediated LED signaling, demonstrating memory-dependent decision-making. These results highlight the M-AS as a versatile neuromorphic platform that combines biodegradability, low-power operation, and learning-based responsiveness—paving the way for sustainable, adaptive electronics and next-generation humanoid robotics.

Methods

Materials

CS (Sigma Aldrich, USA) and GG (High purity chemicals, Korea) were used as the biopolymer components for fabricating the IALs. Acetic acid (AC; Daejung, Korea), 1 N-sodium hydroxide standard (NaOH; Daejung, Korea) were used for pH adjustment and crosslinking of the CS–GG network. NaCl (Sigma Aldrich, USA), lithium chloride (LiCl; Sigma Aldrich, USA), and potassium chloride (KCl; Sigma Aldrich, USA) were utilized as mobile ions in IALs. For IBL, PLA (Goodfellow, England), PCL (Sigma Aldrich, USA), and CA (Sigma Aldrich, USA) were used as biodegradable dielectric materials. These polymers were dissolved in N,N-dimethylformamide (DMF; Sigma Aldrich, USA).

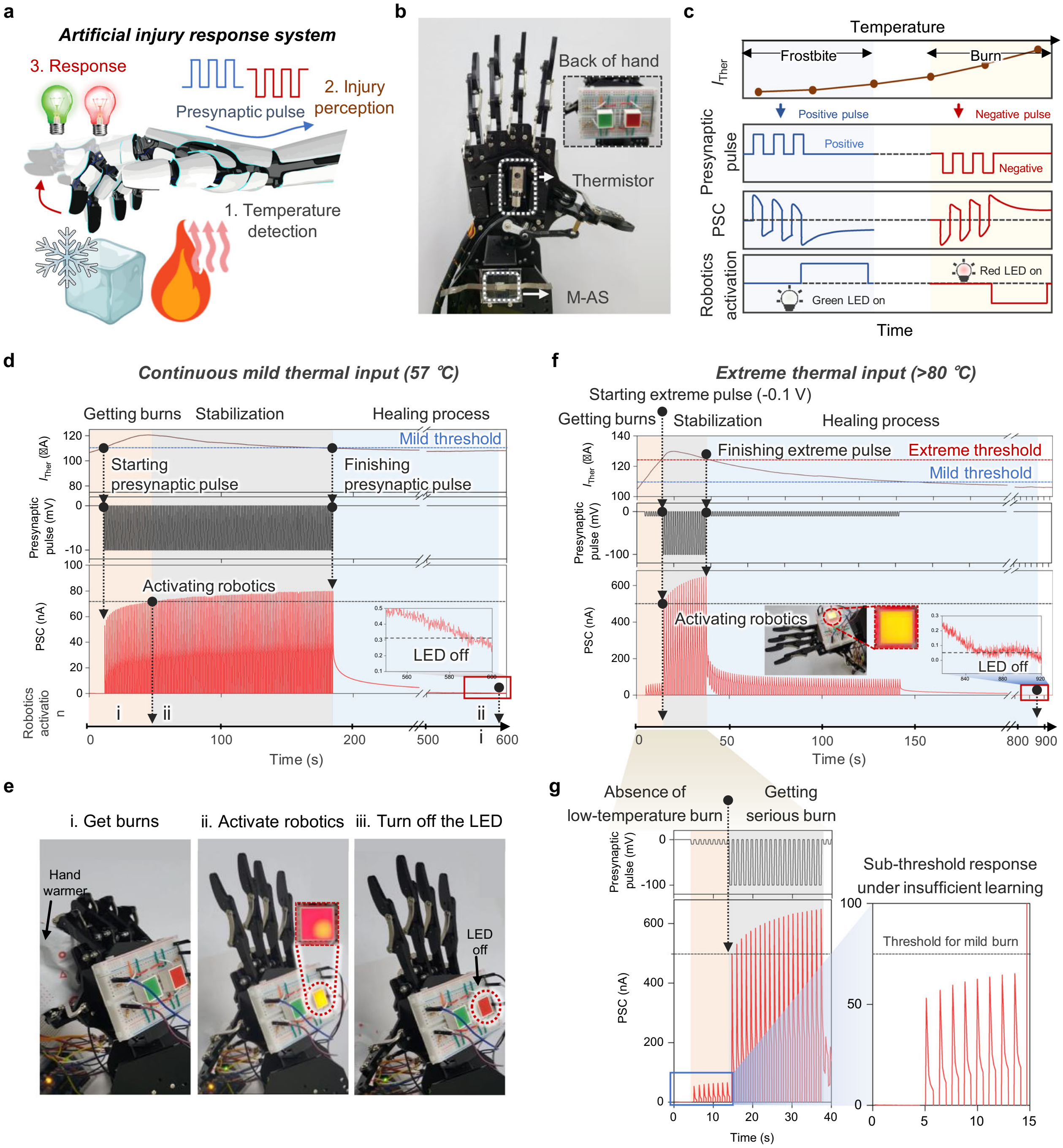

Fig. 6 | Bioinspired artificial injury response system integrating M-AS with thermal sensing and robotic actuation. a Schematic of a bioinspired artificial injury response system integrating a thermistor, M-AS, and a robotic actuator (red/green LEDs and a robotic hand). **b** Photograph of the integrated artificial injury response system composed of a thermistor (sensor), M-AS (synaptic processor), and a robotic hand (actuator); Inset: LEDs mounted on the back of the robotic hand. **c** Signal transduction from temperature sensing to robotic response. The thermistor output current (I_{Ther}) is converted into presynaptic voltage pulses, which trigger PSC generation in the M-AS, subsequently driving robotic actions such as LED activation and finger movement. **d** Real-time PSC response of the M-AS under continuous mild thermal stimulation (57 °C hand warmer), showing gradual synaptic potentiation with low-amplitude presynaptic pulse (− 0.01 V) and activation of one red LED upon exceeding the 130 % PSC threshold with prolonged input over 40 s. The inset shows PSC decay after LTP, emulating the temporal fading of synaptic memory following sustained thermal learning. **e** Photographs of robotic behavior under mild thermal stimulus: **i** learning phase with continuous PSC accumulation by grasping the hand warmer, (ii) burn detection upon PSC threshold crossing, triggering release of the heat source and activation of a single red LED, and (iii) LED turn-off after LTP decay, mimicking time-dependent forgetting. **f** Real-time PSC response and corresponding robotic action under extreme thermal input (> 80 °C), showing rapid PSC increase with high-amplitude presynaptic pulse (− 0.1 V) and simultaneous activation of all four red LEDs. The inset shows the end of LTP marked by a PSC decrease below the initial level. **g** PSC response under sub-threshold thermal stimulation, illustrating insufficient synaptic learning and absence of robotic reaction.

Preparation of IAL

CS (3 wt%) was dissolved in an acidic solution (1.5 v/v% of AC in deionized (DI) water), while GG (1 wt%) was dispersed in DI water. Both solutions were stirred on a 60 °C hot plate for 24 h. The CS and GG solutions were then mixed at a 60:40 weight ratio and stirred at room temperature (RT) for 12 h. After the formation of the homogeneous mixed solution, NaOH was added dropwise under continuous stirring at RT to induce gelation and partial neutralization, resulting in hydrogel formation. The resulting mixture was stirred for an additional 12 h to loosen the aggregated hydrogel and form a double-network polymer solution. NaCl (10 wt% in DI water) was then added to the polymer solution at a final concentration of 3 wt%. Air bubbles were removed using a planetary mixer for 20 min.

Fabrication of the M-AS

The M-AS was fabricated by sequentially stacking layers using a spin-coating process. First, an IAL (0.25 × 0.25 cm^2) was spin-coated onto a PDMS substrate at 500 rpm for 30 s, followed by drying on a 60 °C hot plate for 6 h, resulting in a thickness of ~25 µm. After complete drying, CA (10 wt% in DMF) was stacked by spin-coating (4000 rpm, 30 s) and drying on a 60 °C hot plate for 12 h, yielding a CA thickness of ~3 µm. Finally, another layer of IAL was stacked onto the dried CA using the same process, forming an IAL–IBL–IAL sandwich structure. For the electrical measurements, Mg electrodes were attached using silver paste or deposited via thermal evaporation.

Characterization

The molecular interactions between the crosslinked and non-crosslinked CS and GG were analyzed by an FT-IR spectrometer (670-IR, Varian). Thermal analysis was investigated using a thermogravimetric analyzer (TGA Q500, TA Instruments). Tensile stress–strain curves were acquired using a tensile strain tester (TXA-TM, Yeonjin Corp). Electrical measurements, including voltage pulse application and current response, were performed using a source measure unit (S-2450 sourcemeter, Keithley). The specifications of the source measure unit are summarized in Supplementary Note 8. The stimulation conditions for each experiment are summarized in Supplementary Table 14. EIS measurements were conducted with an impedance analyzer (IM2570, HIOKI) with an AC signal of 100 mV. For the robotic hand (Hiwonder, China) operation under the learning processes, all control sequences were programmed using Python. Real-time data from the sourcemeter was transmitted to a micro-controller unit (Arduino Uno), which was connected in series to the laptop.

DFT calculations

Quantum-mechanical calculations were performed using Gaussian09 with the B3LYP theory level and 6-31 g basis set to evaluate H-bonding strength between CS and GG molecules as well as to determine the molecular dipole moments and electrostatic potential maps of biodegradable dielectric materials. The geometry of the molecular structure was optimized to minimize the energy of the molecule using the Hartree-Fock method and then iteratively solving self-consistent field (SCF) equations. To calculate H-bonding strength between CS and GG, the interaction energy between CS molecules and GG molecules was calculated as follows,

$$E_{\text{Crosslinked CS}-\text{GG}} = E_{\text{Complex CS}-\text{GG}} - E_{\text{CS}} - E_{\text{GG}}$$

where $E_{\text{Crosslinked CS–GG}}$, E_{CS} and E_{GG} are the calculated electronic energies of crosslinked CS–GG, CS, and GG, respectively. Additionally, the Polarizable Continuum Model (PCM) method was used to determine the energy at which molecules electrostatically interact with water. The interaction energies between CS, GG and water were calculated as follows,

$$E_{\text{CS}-\text{water}} = E_{\text{Dissolved CS}} - E_{\text{CS}}$$

$$E_{\text{GG}-\text{water}} = E_{\text{Dissolved GG}} - E_{\text{GG}}$$

where $E_{\text{Dissolved CS}}$, $E_{\text{Dissolved GG}}$, are the calculated solvation energies of CS and GG respectively.

The simulations for PCL–Na$^+$, PCL–Cl$^-$, PLA–Na$^+$, PLA–Cl$^-$, CA–Na$^+$, and CA–Cl$^-$ composites are evaluated to calculate the interaction energy of each dielectric with Na$^+$ and Cl$^-$ ions and provide a quantitative comparison. The interaction energies ($E_{Dielectic-Na^+}$ and $E_{Dielectic-Cl^-}$) were calculated by the following equation:

$$E_{Dielectic-Na^+} = E_{Dielectric/Na^+\,composite} - E_{Dielectric} - E_{Na^+}$$

$$E_{\text{Dielectic}-\text{Cl}^-} = E_{\text{Dielectric}/\text{Cl}^-\text{composite}} - E_{\text{Dielectric}} - E_{\text{Cl}^-}$$

where $E_{\text{Dielectic}-\text{Na}^+}$, $E_{\text{Dielectic}-\text{Cl}^-}$, $E_{\text{Dielectric}}$ E_{Na^+}, and E_{Cl^-} are the calculated electronic energies of dielectric/Na$^+$ and dielectric/Cl$^-$ composites, dielectric, Na$^+$ and Cl$^-$ ions, respectively.

Data availability

All data are available within the article and its Supplementary Information files. Additional data related to this paper may be requested from the corresponding authors. Source data are available in the Figshare database (https://doi.org/10.6084/m9.figshare.30426919)[56].

Code availability

All codes supporting the findings of this study are provided in the Figshare database (https://doi.org/10.6084/m9.figshare.30426919)[56] and are available from the corresponding author upon reasonable request.

References

1. Voglis, G. & Tavernarakis, N. The role of synaptic ion channels in synaptic plasticity. *EMBO Rep.* **7**, 1104–1110 (2006).
2. Kim, S. I. et al. Artificial synapses: dimensionality dependent plasticity in halide perovskite artificial synapses for neuromorphic computing (Adv. Electron. Mater. 9/2019). *Adv. Electron. Mater.* **5**, 1970045 (2019).
3. Kuzum, D., Yu, S. & Wong, H. P. Synaptic electronics: materials, devices and applications. *Nanotechnology* **24**, 382001 (2013).
4. Ramirez, A. & Arbuckle, M. R. Synaptic plasticity: the role of learning and unlearning in addiction and beyond. *Biol. Psychiatry* **80**, e73–e75 (2016).
5. Kim, M.-K. & Lee, J.-S. Short-term plasticity and long-term potentiation in artificial biosynapses with diffusive dynamics. *ACS Nano* **12**, 1680–1687 (2018).
6. Duan, X. et al. Ultralow power, cleft size-adjustable and pH-sensitive hyaluronic acid (HA) biodevices for acid-sensing ion channels emulation. *Small* **20**, 2405207 (2024).
7. Moon, K. et al. Biocompatible neuromorphic device array based on naturally sourced mucin for implantable bioelectronics. *ACS Nano* **19**, 10400–10411 (2025).
8. Zhao, Y., Lee, S., Long, T., Park, H.-L. & Lee, T.-W. Natural biomaterials for sustainable flexible neuromorphic devices. *Biomaterials* **314**, 122861 (2025).
9. Shim, H. et al. Stretchable elastic synaptic transistors for neurologically integrated soft engineering systems. *Sci. Adv.* **5**, eaax4961 (2019).

10. Liang, X., Luo, Y., Pei, Y., Wang, M. & Liu, C. Multimode transistors and neural networks based on ion-dynamic capacitance. *Nat. Electron.* **5**, 859–869 (2022).
11. Chen, J. et al. Imine-based polymeric mixed ionic–electronic conductors featuring degradability and biocompatibility for transient bioinspired electronics. *Angew. Chem. Int. Ed.* **64**, e202417921 (2025).
12. Bhattacharjee, S., Dwivedi, A. & Tiwari, S. P. Development of biodegradable substrates and synaptic transistors for next-generation transient electronics. *Adv. Mater. Technol.* **10**, 2401494 (2025).
13. Yang, Y. et al. Ultraflexible, degradable organic synaptic transistors based on natural polysaccharides for neuromorphic applications. *Adv. Funct. Mater.* **30**, 2006271 (2020).
14. Li, L. et al. Biocompatible acellular dermal matrix-based neuromorphic device with ultralow voltage, ion channel emulation, and synaptic forgetting visualization computation. *ACS Nano* **18**, 31309–31322 (2024).
15. Sun, K., Chen, J. & Yan, X. The future of memristors: materials engineering and neural networks. *Adv. Funct. Mater.* **31**, 2006773 (2021).
16. Choi, D. H. et al. Nature-derived, biocompatible silibinin based bioresorbable neuromorphic device for implantable medical electronics. *Appl. Surf. Sci.* **621**, 156814 (2023).
17. Yan, X. et al. Flexible transparent organic artificial synapse based on the tungsten/egg albumen/indium tin oxide/polyethylene terephthalate memristor. *ACS Appl. Mater. interfaces* **11**, 18654–18661 (2019).
18. Cao, Y. et al. Fully physically transient volatile memristor based on Mg/magnesium oxide for biodegradable neuromorphic electronics. *IEEE Trans. Electron Devices* **69**, 3118–3123 (2022).
19. Lee, J. H. et al. Biocompatible and biodegradable neuromorphic device based on hyaluronic acid for implantable bioelectronics. *Adv. Funct. Mater.* **31**, 2107074 (2021).
20. Sung, M. J. et al. Overcoming the trade-off between efficient electrochemical doping and high state retention in electrolyte-gated organic synaptic transistors. *Adv. Funct. Mater.* **34**, 2312546 (2023).
21. Ke, Y. et al. An artificial electrical-chemical mixed synapse based on ion-gated MoS2 nanosheets for real-time facilitation index tuning. *ACS Appl. Mater. Interfaces* **13**, 15755–15760 (2021).
22. Su, J. et al. Cell–cell communication: new insights and clinical implications. *Signal Transduct. Target. Ther.* **9**, 196 (2024).
23. Liu, Y. et al. Robust sodium carboxymethyl cellulose-based neuromorphic device with high biocompatibility engineered through molecular polarization for the emulation of learning behaviors in the human brain. *ACS Appl. Mater. Interfaces* **16**, 67321–67332 (2024).
24. Rokade, K. A. et al. CogniFiber: harnessing biocompatible and biodegradable 1D collagen nanofibers for sustainable nonvolatile memory and synaptic learning applications. *Adv. Mater.* **36**, 2312484 (2024).
25. Konwar, A., Gogoi, N., Majumdar, G. & Chowdhury, D. Green chitosan–carbon dots nanocomposite hydrogel film with superior properties. *Carbohydr. Polym.* **115**, 238–245 (2015).
26. Konwar, A., Kandimalla, R., Kalita, S. & Chowdhury, D. Approach to fabricate a compact cotton patch without weaving: a smart bandage material. *ACS Sustain. Chem. Eng.* **6**, 5806–5817 (2018).
27. Hosseini, E. S., Manjakkal, L., Shakthivel, D. & Dahiya, R. Glycine–chitosan-based flexible biodegradable piezoelectric pressure sensor. *ACS Appl. Mater. Interfaces* **12**, 9008–9016 (2020).
28. Ge, T. J. et al. A magnetic hydrogel for the efficient retrieval of kidney stone fragments during ureteroscopy. *Nat. Commun.* **14**, 3711 (2023).
29. Sharma, G. et al. Guar gum and its composites as potential materials for diverse applications: a review. *Carbohydr. Polym.* **199**, 534–545 (2018).
30. Rahman, S., Konwar, A., Majumdar, G. & Chowdhury, D. Guar gum-chitosan composite film as excellent material for packaging application. *Carbohydr. Polym. Technol. Appl.* **2**, 100158 (2021).
31. Kim, Y.-R. et al. Bilayer piezoionic sensors for enhanced detection of dynamic, static, and directional forces with self-healing capabilities. *Nano Energy* **127**, 109749 (2024).
32. Wu, X.-L. & Xu, A.-W. Carbonaceous hydrogels and aerogels for supercapacitors. *J. Mater. Chem. A* **2**, 4852–4864 (2014).
33. Sivasankari, S., Kalaivizhi, R., Gowriboy, N., Ganesh, M. R. & Shazia Anjum, M. Hydroxyapatite integrated with cellulose acetate/polyetherimide composite membrane for biomedical applications. *Polym. Compos.* **42**, 5512–5526 (2021).
34. Fahmi, M. Z., Prasetya, R. A., Dzikri, M. F., Sakti, S. C. W. & Yuliarto, B. MnFe2O4 nanoparticles/cellulose acetate composite nanofiber for controllable release of naproxen. *Mater. Chem. Phys.* **250**, 123055 (2020).
35. Kim, Y. et al. Bird-inspired self-navigating artificial synaptic compass. *ACS Nano* **15**, 20116–20126 (2021).
36. Sadgrove, N. J. & Jones, G. L. From petri dish to patient: bioavailability estimation and mechanism of action for antimicrobial and immunomodulatory natural products. *Front. Microbiol.* **10**, 2470 (2019).
37. Cascella, M. & Yasir, A. K. Short-term memory impairment. In: *StatPearls [Internet]*). (StatPearls Publishing, 2024).
38. Zucker, R. S. & Regehr, W. G. Short-term synaptic plasticity. *Annu. Rev. Physiol.* **64**, 355–405 (2002).
39. Hu, L. et al. Ultrasensitive freestanding and mechanically durable artificial synapse with Attojoule power based on Na-Salt Doped Polymer for Biocompatible Neuromorphic Interface. *Adv. Funct. Mater.* **31**, 2106015 (2021).
40. Qiu, R. et al. Bilingual bidirectional stretchable self-healing neuristors with proprioception. *ACS nano* **17**, 12652–12662 (2023).
41. Na, S. et al. Stretchable skin hydration sensor based on hygroscopic and ion conductive polymer composites. *Chem. Eng. J.* **455**, 140957 (2023).
42. Breitsprecher, K., Holm, C. & Kondrat, S. Charge me slowly, I am in a hurry: optimizing charge–discharge cycles in nanoporous supercapacitors. *ACS Nano* **12**, 9733–9741 (2018).
43. Chen, S. et al. Artificial organic afferent nerves enable closed-loop tactile feedback for intelligent robot. *Nat. Commun.* **15**, 7056 (2024).
44. Chen, J. et al. Mimicking neuroplasticity via ion migration in van der Waals layered copper indium thiophosphate. *Adv. Mater.* **34**, 2104676 (2022).
45. Huynh, H. Q. et al. Bio-inspired artificial fast-adaptive and slow-adaptive mechanoreceptors with synapse-like functions. *Adv. Funct. Mater.* **33**, 2303535 (2023).
46. Roh, H. et al. Unraveling polymer–ion interactions in electrochromic polymers for their implementation in organic electrochemical synaptic devices. *Adv. Funct. Mater.* **33**, 2304893 (2023).
47. Zhang, J. et al. Artificial synapse based on bio-hierarchical porous memristor driven by multilevel-ions migration. *Adv. Electron. Mater.* **8**, 2200269 (2022).
48. He, K. et al. Artificial neural pathway based on a memristor synapse for optically mediated motion learning. *ACS Nano* **16**, 9691–9700 (2022).
49. Wang, M. et al. Retinoic acid-poly (lactic) acid composite for biocompatible optoelectronic synapses with flexible curvature detection and biomimetic imprinting capabilities. *ACS Mater. Lett.* **6**, 1999–2006 (2024).
50. Sueoka, B., Cheong, K. Y. & Zhao, F. Natural biomaterial honey-based resistive switching device for artificial synapse in neuromorphic systems. *Appl. Phys. Lett.* **120**, 083301 (2022).

51. Park, Y. & Lee, J.-S. Artificial synapses with short-and long-term memory for spiking neural networks based on renewable materials. *ACS nano* **11**, 8962–8969 (2017).
52. Raeis-Hosseini, N., Park, Y. & Lee, J. S. Flexible artificial synaptic devices based on collagen from fish protein with spike-timing-dependent plasticity. *Adv. Funct. Mater.* **28**, 1800553 (2018).
53. Yoon, J. H. et al. An artificial nociceptor based on a diffusive memristor. *Nat. Commun.* **9**, 417 (2018).
54. Benda, J. Neural adaptation. *Curr. Biol.* **31**, R110–R116 (2021).
55. Evers, L. H., Bhavsar, D. & Mailänder, P. The biology of burn injury. *Exp. Dermatol.* **19**, 777–783 (2010).
56. Chang, Y. et al. Source data for "Robust Biodegradable Synapse with Sub-Biological Energy and Extended Memory for Intelligent Reflexive System." *Figshare*. https://doi.org/10.6084/m9.figshare.30426919 (2025).

Acknowledgements

Y. Chang, S. Na, and Y.G. Ro contributed equally to this work. This work was supported by the National Research Foundation (NRF) of Korea (RS-2021-NR059784).

Author contributions

H.K. conceived the project. Y.C. and S.N. designed the experiment and fabricated the devices. Y.G.R. S.J., and M.S.K. designed the simulation system and performed simulation characterization and analysis. Y.C., S.N., and Y.G.R. performed measurement, characterization, and analysis. C.P. aided in the fabrication of robotic systems. Y.C., Y.J.P., J.K., H.O., and J.K. discussed and analyzed the data. H.K. supervised the overall conception and design of this study. Y.C., S.N., Y.G.R., and H.K. wrote the paper, on which all authors provided feedback.

Competing interests

The authors declare no competing interests.

Additional information

Supplementary information The online version contains supplementary material available at https://doi.org/10.1038/s41467-025-66511-3.

Correspondence and requests for materials should be addressed to Hyunhyub Ko.

Peer review information *Nature Communications* thanks Tukaram Dongale, and the other, anonymous, reviewer(s) for their contribution to the peer review of this work. A peer review file is available.